Eur. Phys. J. D **26**, 173–185 (2003)
DOI: 10.1140/epjd/e2003-00221-7

THE EUROPEAN PHYSICAL JOURNAL D

Observation of the long-range potential well of the $(6)^1\Sigma_g^+(3s+5s)$ state of Na_2

T. Laue[1], P. Pellegrini[2], O. Dulieu[2,a], C. Samuelis[1], H. Knöckel[1], F. Masnou-Seeuws[2], and E. Tiemann[1,b]

[1] Institut für Quantenoptik, Universität Hannover, Welfengarten 1, 30167 Hannover, Germany
[2] Laboratoire Aimé Cotton, CNRS, Campus d'Orsay, Bâtiment 505, 91405 Orsay Cedex, France

Received 5 March 2003
Published online 22 July 2003 –

Abstract. We report on the first observation of the outer well of the $(6)^1\Sigma_g^+$ state of Na_2 molecule. The levels are populated in a molecular beam experiment with a three step laser excitation. The fact that these levels predissociate allows an almost background free detection by the appearance of atomic fluorescence. With this method almost all vibrational levels of the outer well are observed. The corresponding predissociation line widths show an oscillating behaviour. The theoretical description of the predissociation is presented in the framework of mapped Fourier grid Hamiltonian representation with optical potential, involving two coupled electronic states. Combining the spectroscopic information on energy positions and predissociation widths, a Rydberg-Klein-Rees potential curve is given for the outer well. Such a state could offer a reliable path for photoassociation of cold Na atoms and formation of ultracold Na_2 molecules.

PACS. 33.80.Gj Diffuse spectra; predissociation, photodissociation – 31.50.Gh Surface crossings, non-adiabatic couplings – 42.62.Fi Laser spectroscopy

1 Introduction

Excited potential curves of diatomic alkali molecules may show a double well structure, which have been observed experimentally in a few cases [1–4]. Potentials with such a special shape play an important role for the production of cold ground state molecules and their study is of particular interest. Indeed, laser cooling techniques, which are successfully used for atoms, can generally not be extended to molecules due to their dense level structure of each electronic state. One solution consists in forming cold molecules by photoassociation of two previously cold atoms into an excited electronic state followed by spontaneous emission to the molecular ground state. To increase the efficiency of the spontaneous emission step, the population of bound states of an outer well of excited molecular potentials is very favourable because the Franck-Condon overlap with ground state levels is enhanced by the amplitude of the vibrational wave function in the double well at intermediate internuclear separation [5].

Photoassociation experiments using cold Na atoms have been achieved some years ago [6], but the observation of ultracold Na_2 molecules [7] is not favoured by the existing long-range potential wells correlated to the $3s+3p$ limits, in contrast with Rb_2 [8] and Cs_2 [5]. The search for more favourable scheme is therefore a challenge. For instance, *ab initio* calculations by Magnier *et al.* [9] predict the existence of a secondary well for the $(6)^1\Sigma_g^+$ state of Na_2 molecule around $35a_0$ ($a_0 = 0.0529177$ nm) which results from a configuration change of the electronic wavefunction from ionic to covalent character.

Such an electronic state could be used to create cold Na_2 molecules, and it is the purpose of the present paper to provide the accurate spectroscopy of this state.

The inner well of the $(6)^1\Sigma_g^+$ state in Na_2, which correlates to the $3s+5s$ asymptote, was studied with optical-optical double resonance spectroscopy [10]. The highest observed level lies near the energy of the local minimum of the outer well, according to the *ab initio* calculations of reference [9], but is well separated from the outer well by a fairly high barrier. Starting from the same calculations, a detailed theoretical investigation of the outer well was performed by Almazor *et al.* [11]. In addition to the calculation of eigenenergies of the outer well of the $(6)^1\Sigma_g^+$ state, the possibility to populate this well starting from ground state molecules was discussed.

In this paper we report on the observation of the second well of the $(6)^1\Sigma_g^+$ state in a molecular beam experiment using a three step laser excitation. After a description of the experimental setup (Sect. 2), we present the experimental results (Sect. 3), and explain the extraction of a potential curve for the outer well (Sect. 4). A model of two coupled electronic states, the $(6)^1\Sigma_g^+$ with the $(5)^1\Sigma_g^+$, (Sect. 5) is used to describe the observed predissociation of the levels of the outer well into the

[a] e-mail: dulieu@lac.u-psud.fr
[b] e-mail: tiemann@iqo.uni-hannover.de

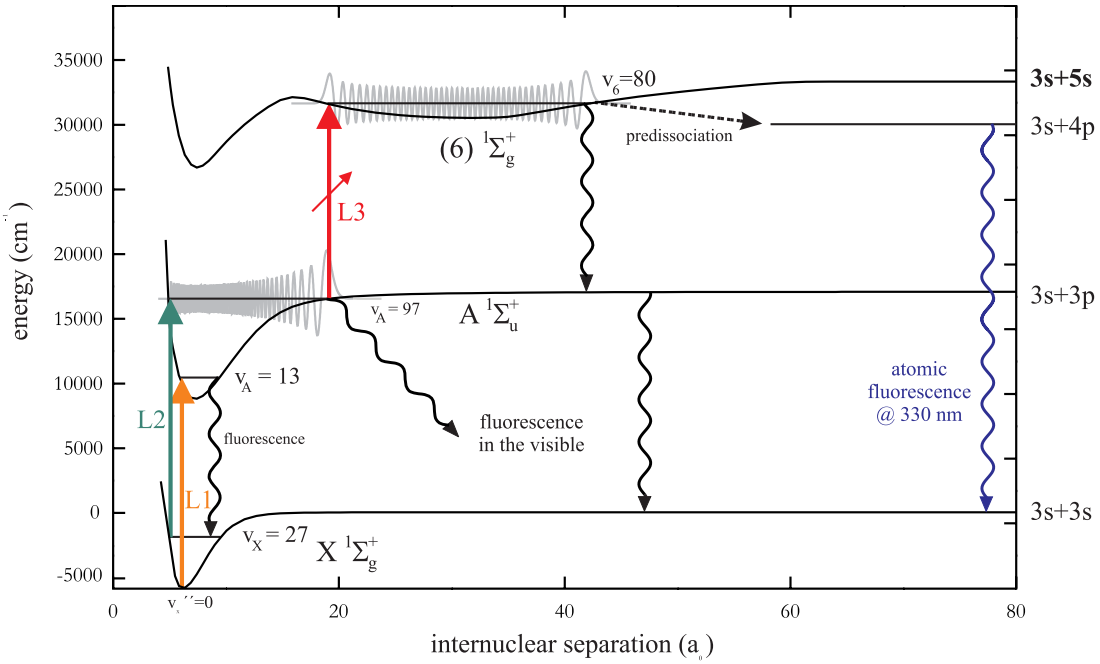

Fig. 1. Experimental excitation scheme to access levels of the outer well of the $(6)^1\Sigma_g^+(3s+5s)$ state of Na_2.

$3s+4p$ dissociation continuum, and is compared with the experiment.

2 Experimental setup

The levels of the second well of the $(6)^1\Sigma_g^+$ state are observed using a multistep laser excitation scheme, starting with molecules in a well-collimated beam where mainly the few lowest vibrational ground state levels ($v_X = 0$, 1, and 2) are populated. A sketch of the excitation scheme is given in Figure 1. A first laser L1 around 620 nm is kept on an appropriately chosen rovibrational transition between the $A^1\Sigma_u^+$ state and the $X^1\Sigma_g^+$ ground state (*e.g.* $X(v_X = 0, J) \rightarrow A(v_A = 13, J+1)$) to populate higher vibrational levels (*e.g.* $v_X = 27$) by Franck-Condon pumping in a first interaction zone. For long-term stability this laser is locked on the maximum of the fluorescence which is monitored by a photomultiplier.

Starting from these levels it is possible to populate with a two-photon process levels of the outer well of the $(6)^1\Sigma_g^+$ state using two additional lasers. The second laser L2 around 530 nm is resonant with a transition from a Franck-Condon pumped level to a high lying vibrational level of the A state [12]. For this study the vibrational levels $v_A = 88$ to 122 were used as intermediate levels. The long-term stability of laser L2 is ensured by a stabilization on a external Fabry-Perot interferometer with a free spectral range of 150 MHz, which has a fixed frequency comb due to stabilization to an iodine-stabilized He-Ne laser. For interpolation between the fringes of this coupling cavity the frequency of the He-Ne lasers can be shifted with an AOM.

The third laser L3 is used to excite levels of the outer well at their inner turning point, as it is indicated in Figure 1. Wavelengths between 625 nm to 735 nm are necessary for this step. While laser L3 is tuned, the molecular fluorescence out of the intermediate A state level back to the ground state and the atomic fluorescence of the transition $4p \rightarrow 3s$ at 330 nm is observed. If laser L3 hits the two-photon resonance, due to the predissociation of the upper level into the continuum above the $3s+4p$ asymptote, a signal by atomic fluorescence at 330 nm is observed. This detection scheme is almost background-free because the frequency of this atomic fluorescence is far away from all laser frequencies involved or from molecular fluorescence. It was not possible to observe any two photon signal on the molecular detection channel under our experimental conditions. Populating levels of the $(6)^1\Sigma_g^+$ state did not lead to a significant reduction of the molecular fluorescence from the intermediate level, in contrast to a previous experiment accessing the ground state asymptotes of Na_2 [13].

The experimental setup is similar to the one given in [13]. The three laser beams intersect the collimated molecular beam in two interaction zones perpendicularly. The first zone for the Franck-Condon pumping with laser L1 is separated from the second one, where laser L2 and L3 are spatially overlapped, to avoid multi-photon processes including all three lasers. All lasers are tunable single-mode dye lasers which are operated with sulforhodamin (L1), coumarin 6 (L2) and DCM or pyridin 2 (L3). For the simultaneous observation of the molecular and atomic fluorescence in the second interaction zone, the total fluorescence is collected by a lens system, splitted by a dichroitic beam splitter into a visible and an ultra-violet part, and focussed onto two different photomultipliers.

The energies of the observed levels will be referred to the lowest hyperfine asymptote $3s(f=1) + 3s(f=1)$ of

the molecular ground state. Therefore several frequency calibration steps are necessary. The energetic distance between $v_X = 0, J_X = 0$ and $v_X = 27, J_X = 0$ was derived from measurements by Wang [14] with an uncertainty of ≈ 30 MHz. Starting from this level we measured with laser L2 several transitions of the $A - X$ system with iodine saturation spectroscopy to determine energy differences of rotational or vibrational levels of the ground state. With this method it is possible to calibrate within several steps the Franck-Condon pumped levels of the $X^1\Sigma_g^+$ state which were used for this experiment. The frequencies of the hyperfine resolved iodine lines are calculated with the program *Iodinespec*, which gives a 2σ prediction uncertainty of 3 MHz [15]. Together with the comb of a 150 MHz Fabry-Perot cavity, whose free spectral range is known with an uncertainty of less than 10 kHz, we reach an overall uncertainty of 10 MHz for the transition frequencies of the $A - X$ system. With the same setup the frequencies of laser L2 are calibrated, which are used to populate the desired intermediate level in the A state prior to the excitation of levels of the outer well of the $(6)^1\Sigma_g^+$ state. For the determination of the frequency of the laser L3, we use iodine absorption spectroscopy and the 150 MHz cavity for interpolation. Again the iodine lines were calculated with the program *Iodinespec*, but this time with unresolved hyperfine structure, *i.e.* with an absolute accuracy of about 60 MHz. This calibration procedure leads to term energies of the levels of the $(6)^1\Sigma_g^+$ state with respect to the level $v_X = 0, J_X = 0$ of the $X^1\Sigma_g^+$ ground state. To refer these energies to the $3s(f = 1) + 3s(f = 1)$ asymptote one has to subtract the energetic difference 5942.6148(39) cm^{-1} between $v_X = 0, J_X = 0$ and $3s(f = 1) + 3s(f = 1)$ [13]. This gives a minimum 1σ uncertainty of the level energies referred to $3s(f = 1) + 3s(f = 1)$ of 0.005 cm^{-1}. In cases of low signal-to-noise ratio or levels broader than 2.8 GHz of $(6)^1\Sigma_g^+$ this will increase, but will never be larger than 0.008 cm^{-1}.

3 Measurements

With the above setup we measured 105 vibrational levels of the outer well of the $(6)^1\Sigma_g^+$ state up to the internal barrier and a few levels covering both wells of the double minimum potential. For all levels, the observation relies on the predissociation observed through atomic fluorescence. In the following quantum numbers with index 6 belong to levels of the outer well of the $(6)^1\Sigma_g^+$ state. The data set mainly contains levels with rotational quantum numbers $J_6 = 9$ and $J_6 = 11$, corresponding to $J_A = 10$ for the intermediate level in the $A^1\Sigma_u^+$ state. For a few vibrational levels $J_A = 19$ was used as intermediate one as well and for one vibrational level the whole rotational ladder from $J_6 = 0$ to $J_6 = 20$ was measured[1].

[1] All our data are available on request. These data contain the assignment (for the vibrational quantum number see discussion below), the energetic positions of the levels referred to the $3s(f = 1) + 3s(f = 1)$ asymptote (see Sect. 2), and the linewidth of the level.

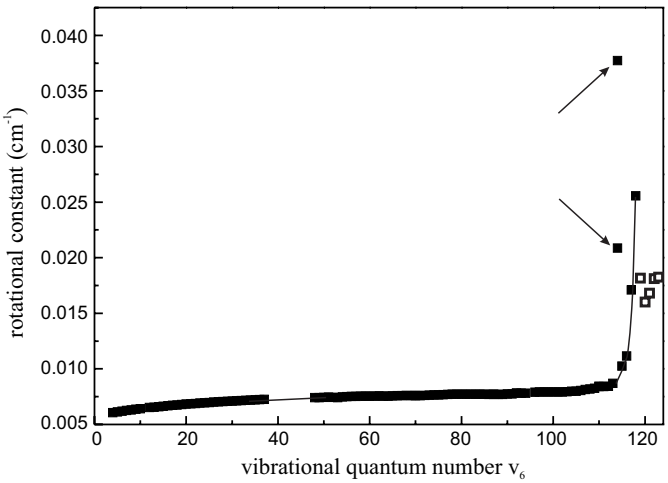

Fig. 2. Rotational constants derived from the doublet $J_6 = 9$ and $J_6 = 11$ for the vibrational levels lying entirely within the $(6)^1\Sigma_g^+$ outer well (solid squares), or above the potential barrier between the two wells (open squares). A solid line connects all points, to make clear the variation. The assignment of the vibrational quantum number will be discussed in Section 4. Levels marked by arrows are tunneling levels (see text for explanation).

Figure 2 shows rotational constants of the levels of the $(6)^1\Sigma_g^+$ outer well derived from the splitting of the rotational doublet $J_6 = 9$ and $J_6 = 11$ as a function of the vibrational quantum number v_6 (the vibrational assignment is discussed in Sect. 4). The rotational constant increases gradually from 0.006 cm^{-1} for low v_6 to 0.008 cm^{-1} for v_6 around 100. This variation differs from the decreasing behaviour of a normal molecular oscillator and reflects the unusual shape of this well. Close to the top of the barrier between both potential wells the rotational constant increases rapidly to a value of 0.026 cm^{-1}, due to the opening of the outer well to smaller internuclear distances. This behaviour which is made clear by a connecting line in Figure 2 has two exceptions, marked by arrows and discussed below. Around $v_6 = 40$, 10 vibrational levels were not observed due to the lack of appropriate laser sources. Unfortunately, it was not possible with our equipment to connect the wavelength range of the dye pyridin 2 to that of DCM without any gap. The connecting line in Figure 2 indicates the expected behaviour of the rotational constant in this energetic region. Because of the known vibrational spacing below and above this gap there is no doubt concerning the number of missing levels and therefore the relative assignment of the vibrational levels is fixed.

Figure 2 also contains a few rotational constants which belong to levels extending over the whole double well potential (open squares). The given vibrational assignment of the levels above the barrier is just a continuation of the vibrational quantum numbers of the outer well because the inner well is not known up to the barrier. Evidence for the observation of levels above the barrier is provided by the abrupt change of the rotational constant which is proportional to the inverse of the moment of inertia.

Therefore, levels above the barrier have larger values for the rotational constant than for the levels of the outer well because the wavefunctions of the outer well are located at larger internuclear separations. The excitation scheme applied needs a good amplitude of the vibrational wavefunction at intermediate internuclear separations, *e.g.* $18a_0$ in Figure 1. Thus levels far above the barrier will be hardly excited in the present setup. This limited the number of observed levels above the barrier to five.

Just below the barrier for $v_6 = 114$ two levels for each $J_6 = 9$ (level energies 31942.268(9) cm^{-1} and 31944.304(6) cm^{-1}) and $J_6 = 11$ (level energies 31943.149(9) cm^{-1} and 31945.889(6) cm^{-1}) were observed, which give exceptional rotational constants (marked in Fig. 2 with arrows). Their spacing of only ≈ 2 cm^{-1} is substantially smaller than the local vibrational frequency of approximately 11 cm^{-1} (the vibrational spacing decreases to about 8 cm^{-1} just below the top of the barrier). This behaviour can be explained by tunneling through the potential barrier between the inner and the outer well. If two levels of each well are almost degenerate, the probability for tunneling through a not too wide barrier is very high and both levels repel each other. Due to the tunneling the wavefunction is located in both potential wells which leads to larger rotational constants of these levels compared to levels of the outer well. From the magnitude of the rotational constant, one can distinguish whether the wavefunction of these two levels has a larger amplitude in the inner or outer well, respectively. Similar tunneling was observed in Cs_2 in a photoassociation experiment [16].

If one performs the same experiment using an intermediate level with a different angular momentum, the resonance condition for tunneling will be different. We observed rovibrational levels close to the barrier for $v_6 = 114$ and $J_6 = 18$ and $J_6 = 20$ as well. In this case the rotational constant is quite normal again. The tunneling rate is strongly J dependent and is too small for $J_6 = 18$ and $J_6 = 20$. For $v_6 = 115$, however, for $J_6 = 18$ and 20 again an unexpected large rotational constant was found, but with the current signal-to-noise ratio no additional lines of a tunneling doublet could be detected. From these levels information about the inner potential well could principally be derived, but there remains a large gap to the uppermost observed level in the inner well. So a detailed characterisation of the inner well is not an easy task and will not be pursued in this paper.

The observation of the outer well should be compared with *ab initio* calculations. A comparison of the observed rotational constants (see Fig. 2) and vibrational spacings with the calculated ones reported by Almazor *et al.* [11], which are based on *ab initio* potentials [9], leads to an agreement for the rotational constants within the experimental uncertainty while the calculated vibrational spacings are slightly too large. For vibrational spacings lying within the 12 cm^{-1} to 14 cm^{-1} range, the deviation between experiment and *ab initio* calculation is always -0.1 cm^{-1} whereas for levels close to the potential minimum and to the top of the barrier this deviation increases up to -0.4 cm^{-1}. Nevertheless the agreement between observation and calculation is good for finding easily the neighbouring vibrational levels once a vibrational level of the outer well of the $(6)^1\Sigma_g^+$ state has been observed.

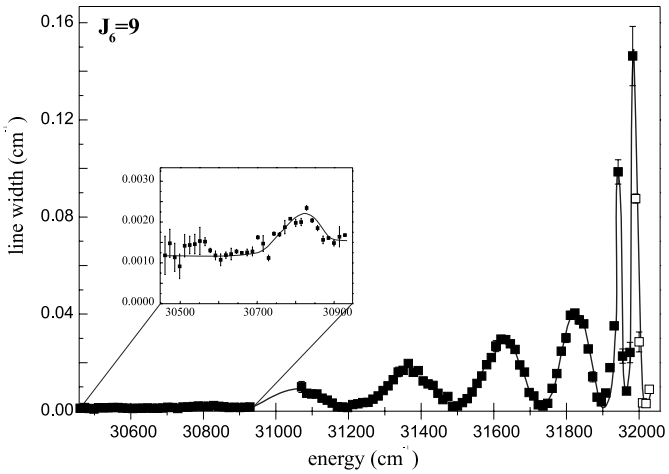

Fig. 3. Observed line widths of the vibrational levels (with $J_6 = 9$) lying within the $(6)^1\Sigma_g^+$ outer well (solid squares), or above the potential barrier (open squares). The origin of energy is taken at the $3s(f = 1) + 3s(f = 1)$ asymptote. A solid line connects all points, to make clear the variation.

Up to now only the energetic positions of the levels of the outer well were discussed, but as already mentioned the detection scheme relies on the predissociation of these levels. Therefore, the line widths of the levels of the outer well is of special interest because they directly indicate the predissociation rate. Almazor *et al.* [11] estimated predissociation lifetimes with a Landau-Zener model and predicted a continuous decrease with increasing energy.

As shown in Figure 3 the observed line widths depend on the energy and oscillate faster and faster as the energy approaches the internal barrier. The narrowest line has a width of 30 MHz, the broadest 4.4 GHz. With each oscillation the maximum line width increases, and so does the line width at the minima of the oscillations.

The energy reference in Figure 3 is again the $3s(f = 1) + 3s(f = 1)$ asymptote. The last data points indicate that the line width oscillation probably continues above the barrier. The gap between 30930 cm^{-1} and 31070 cm^{-1} corresponds to the same region as in Figure 2 and the line suggests the expected behaviour of the line widths. The insert shows with enlarged scale the line widths for the lowest 35 observed vibrational levels. Here another maximum for the line widths becomes visible.

These widths are directly taken from the experimental observation which means that, in addition to the predissociation broadening, they contain other contributions like natural radiation width, laser line width (≈ 1 MHz), time of flight broadening and residual Doppler width. Under our experimental conditions (focus diameter ≈ 200 μm), the time of flight broadening is in the order of a few MHz, but the largest contribution to the experimental broadening is the residual Doppler width of the two-photon transition with $\approx$15 MHz. In addition, the levels of the outer

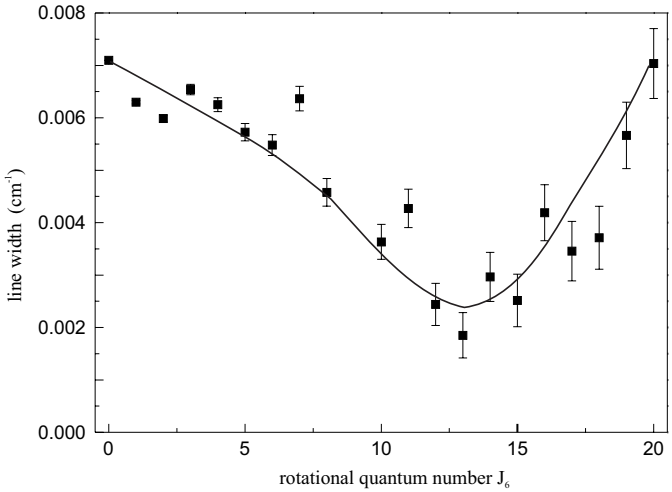

Fig. 4. Rotational dependence of the observed line widths of the vibrational level $v_6 = 77$ for $J_6 = 0$ to $J_6 = 20$.

well can decay radiatively. The calculated rate [11] is in the order of a few 10^{-6} s and therefore this contribution to the width is smaller than 1 MHz.

If the signal-to-noise ratio is sufficient, the linewidth given is simply the full line width half maximum of the observed symmetric profile, otherwise the line profile is fitted. For broad lines close to the internal barrier we assumed a Lorentzian profile and for narrow lines close to the potential minimum the profile is better described by a convolution of a Gaussian and Lorentzian profile.

The observed line width oscillation for $J_6 = 11$ is almost exactly the same as the depicted one in Figure 3 for $J_6 = 9$. The influence of rotation on the line width is small compared to its vibrational dependence since the energy variation is smaller. For one vibrational level, which is close to the minimum of the line width at 31500 cm^{-1} ($v_6 = 77$), we studied the line width depending on the angular momentum J_6 in more detail (see Fig. 4). Starting with $J_6 = 0$ the line width drops down from 210 MHz to 55 MHz for $J_6 = 13$, followed by an increase up to again 210 MHz for $J_6 = 20$. Scaling the abscissa by energy the graph corresponding to Figure 4 has symmetrical appearance.

4 Potential determination

In the previous section an assignment of the observed vibrational levels was already assumed. But in contrast to the rotational quantum number, which is determined by the chosen intermediate level, a purely experimental assignment of the vibrational quantum number is not obvious. The assumption that the lowest observed level is the vibrational level $v_6 = 0$ will be incorrect in most cases, especially because the detection of the levels relies on the predissociation rate which is decreasing while approaching the potential minimum of the outer well. Additionally, the laser power was limited in our setup to only a few mW in the frequency range which is needed to excite the low lying vibrational levels. This might be not sufficient for the two-step excitation.

To get more information on the vibrational assignment we measured the line intensities of transitions to a single low-lying vibrational level of the outer well from different vibrational levels of the $A^1\Sigma_u^+$ state as intermediate level. The line intensities are normalized to the laser intensity to compare them with Franck-Condon factors for transitions between the A state and the outer well of the $(6)^1\Sigma_g^+$ state. For the calculation of the Franck-Condon factors we used a Rydberg-Klein-Rees (RKR) potential for the A state which was derived from known data from the literature and own measurements. For the outer well of $(6)^1\Sigma_g^+$, RKR potentials for different vibrational assignments were constructed *via* Dunham parameters, approximating the outer well as a normal potential with repulsive branch, neglecting the effects of the barrier and the inner well. The assignment giving the best agreement between calculated Franck-Condon factors and measured intensities was used, but an uncertainty of ± 1 unit remains. The lowest observed level then gets the quantum number $v_6(min) = 4$ for the outer well.

The best RKR potential is then represented analytically by a power series [17]:

$$V(R) = T_m + a_1\xi + a_2\xi^2 + a_3\xi^3 + ..., \qquad (1)$$

with

$$\xi = \xi(R, b) = \frac{R - R_m}{R + bR_m}, \qquad (2)$$

where R_m is the equilibrium distance of the initial RKR potential and the parameters b, T_m, a_1, ... are determined from a least squares fit to the RKR potential. The parameter b in equation (2) is used to handle the very different steepness of the potential left and right to R_m and is chosen such that the number of a_i coefficients required to represent the RKR potential is minimal. This representation is extended with an exponential repulsive branch for $R < 16.1a_0$ and by a dispersion term from $R > 42.5a_0$ to larger internuclear distances. It was checked that the eigenenergies of the considered levels determined numerically in this potential were affected by not more than their experimental uncertainty by these extensions and by neglect of the barrier and the inner well. We note that the highest observed levels, *i.e.* levels between $v_6 = 100$ and $v_6 = 118$, were excluded, because the model for the potential is designed for a single well only and cannot handle the bend close to the barrier.

The parameters T_m and a_i are then refined by minimizing the differences between the experimental energy levels and those calculated numerically using a Numerov method, where we chose a $0.0074a_0$ grid spacing in order to get sufficiently fine spatial resolution of the vibrational wavefunctions also for high v_6.

With the vibrational assignment derived above a fit of the analytical potential including all observed vibrational levels up to $v_6 = 100$ gives a normalized standard deviation $\sigma = 4.2$. The differences (obs-cal) between observed and calculated values for this potential oscillate around zero depending on the vibrational quantum number just

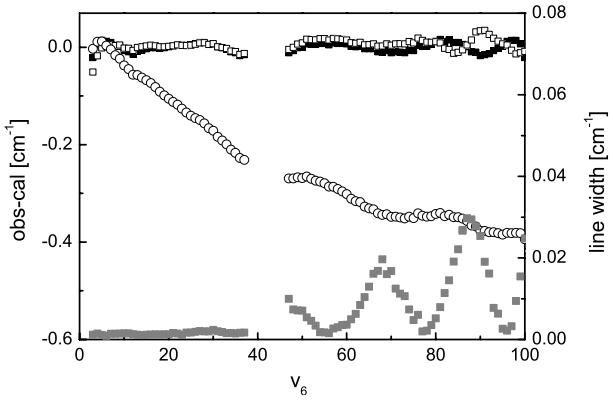

Fig. 5. Vibrational dependence of (obs-cal) of energies for a single channel potential fit with vibrational quantum number reduced by one with respect to determination from Franck-Condon factors (see text). The energy deviations (black squares, left scale) oscillate like the linewidth (grey squares, right scale). A coupled channel calculation with two states gives an increasing systematic deviation due to the interaction (open circles). This can be iteratively reduced (see Sect. 5.5), but the oscillation in (obs-cal) cannot be removed (open squares).

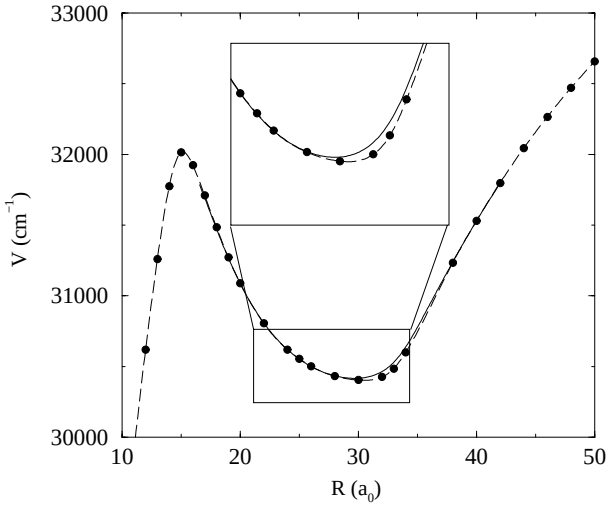

Fig. 6. Constructed potential curve derived from experiment (solid line), and theoretical curve from reference [9] (dots and dashed line) for the $(6)^1\Sigma_g^+$ outer well. The energy origin is taken at the the $3s+3s$ asymptote. The region of the potential minimum is blown up in the inset. The experimental curve is matched to the theoretical one below $15a_0$.

like the predissociation line widths do. Additionally, levels close to the gap between $v_6 = 38$ and $v_6 = 48$ and close to the potential minimum show quite large deviations in (obs-cal).

The fit quality improves rather abruptly if the assignment is changed to $v_6(min) = 3$ instead of $v_6(min) = 4$ for the lowest observed level. The standard deviation decreases to $\sigma = 2.1$. Nevertheless the oscillation in (obs-cal) remains, but with a smaller amplitude, and the levels close to the boarder of the measurements are better described as well (full squares in Fig. 5).

Further shift of the vibrational assignment towards lower values improves the fit quality just a little bit, but if one assumes that the lowest observed level is $v_6 = 0$ the standard deviation increases again. Therefore the present approach of an analytic potential apparently cannot give a unique assignment but it seems probable that the vibrational assignment has to be shifted compared to the result obtained *via* Franck-Condon factors by at least one and at most by three units to lower values. An assignment adding one or two units leads to a significant deviation between observation and calculation. The assignment of $v_6(min) = 3$ is used for the Fourier grid calculations described in Section 5.

In Figure 6, the analytic potential, and the external well of the adiabatic potential calculated in reference [9] are compared. Both potentials are referred to the energy origin at $3s + 3s$. The two potentials are quite well superimposed, while they differ at most by 15 cm^{-1} at the bottom of the well.

Due to the observed predissociation it is clear that a coupling to at least one other electronic state exists but the potential one derives by the procedure above does not include the coupling. Nevertheless this potential can be used as a first approximation for more refined calculations which will be described in the following section.

5 Theoretical description

The predissociation of the vibrational levels lying in the $(6)^1\Sigma_g^+(3s+5s)$ external well, due to the interaction with the $(5)^1\Sigma_g^+(3s+4p)$ electronic state has been previously analyzed in reference [11], in the framework of a simple Landau-Zener semiclassical picture for the avoided crossing between these two states. A structureless increase of the predissociation probability with decreasing binding energy was predicted and has been used as a guide for the detection efficiency in the present experiment. In this section, we investigate the predissociation process in more details, in order to interpret the observed oscillations in the experimental linewidths. We solve directly the coupled Schrödinger equations through the mapped Fourier grid Hamiltonian (MGFH) representation [18–22] using an adaptive coordinate [23,24], and a complex absorbing potential [25–28].

5.1 The Hamiltonian of the system

As discussed above, and in reference [29], the double-well structure of the $(6)^1\Sigma_g^+$ state results from the interaction between covalent configurations (of $3s+nl$ type) and ionic configuration arising mainly from $Na^+ + Na^-(^1S)$. The ionic potential curve behaves as $1/R$ and crosses all covalent configurations, inducing a series of avoided crossings in the Born-Oppenheimer adiabatic potential curves (Fig. 7).

A diabatic representation of the electronic states of Figure 7 has been determined in reference [29]. Figure 8a displays these results for the $^1\Sigma_g^+$ symmetry, in the vicinity of the avoided crossing studied here. These calculations rely on a diabatization procedure, which consists in

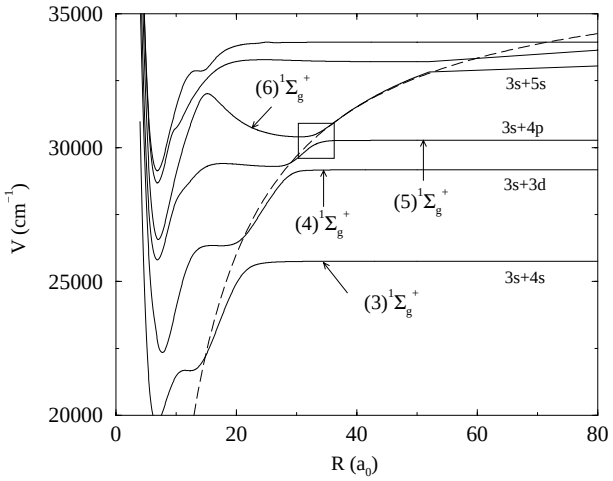

Fig. 7. Adiabatic $^1\Sigma_g^+$ potential curves of Na_2, as calculated in reference [9]. The origin of energy is the $3s+3s$ asymptote. The dashed curve sketches the ionic $Na^+ + Na^-(^1S)$ configuration varying as $1/R$, which is traced by a series of avoided crossings. The avoided crossing studied here is marked by the square. The avoided crossings beyond 60 a_0 are not distinguishable.

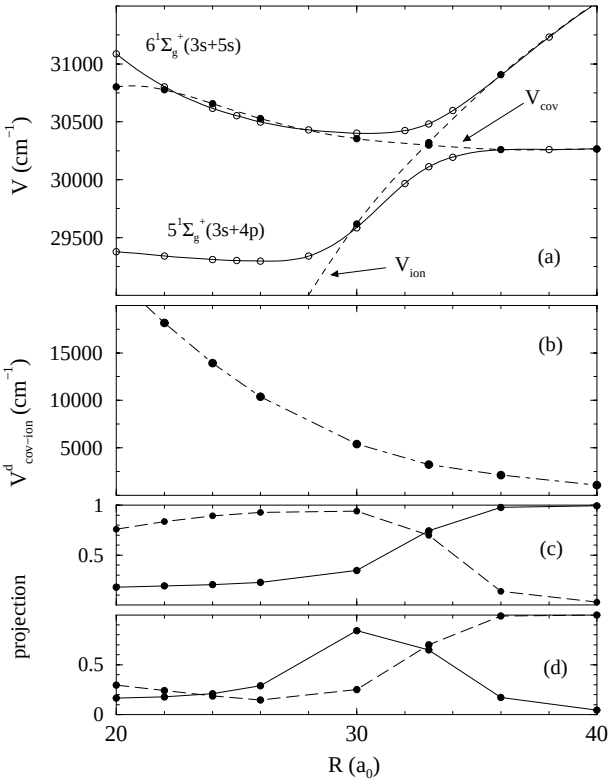

Fig. 8. Adiabatic and diabatic calculations from reference [29]. (a) Adiabatic potentials (full lines) for the $(5)^1\Sigma_g^+$ and $(6)^1\Sigma_g^+$ coupled states, and corresponding diabatic potentials (dashed lines) for the covalent ($V_{\rm cov}$) and ionic ($V_{\rm ion}$) channels, correlated respectively to the $3s+4p$ and $Na^+ + Na^-(^1S)$ configurations at large distances. (b) Interaction term between $V_{\rm cov}$ and $V_{\rm ion}$. (c) Projection of the $(6)^1\Sigma_g^+$ adiabatic state on the ionic (full line) and covalent (dashed line) channel. (d) *Idem* for the $(5)^1\Sigma_g^+$ adiabatic state.

an orthonormalized projection of a restricted set of adiabatic electronic states (the 10 lowest adiabatic states in Ref. [29]), over a basis of non-orthogonal wave functions constructed as antisymmetrized products of atomic wave functions localized on each Na atom, and corresponding to the lowest dissociation limits $Na(3s)+Na(nl)$ and $Na(3p)+Na(3p)$ (10 covalent configurations in total in Ref. [29]), and the ionic dissociation limit $Na^+ + Na^-(^1S)$. The system is now represented by an effective diabatic Hamiltonian matrix $\mathbf{H}^{\rm diab}$, whose diagonal elements are interpreted as diabatic energies (dashed curves in Fig. 8a). The avoided crossing in Figure 7 marked by the open square clearly results from the interaction between a covalent curve $V_{\rm cov}$ correlated to the $3s+4p$ limit, with the ionic curve $V_{\rm ion}$ associated to $Na^+ + Na^-(^1S)$. The non-diagonal element $V^d_{\rm cov-ion}$ of $\mathbf{H}^{\rm diab}$ connecting $V_{\rm cov}$ and $V_{\rm ion}$ is drawn in Figure 8b: it is slowly varying around the crossing, and is not symmetric. Let us note that its amplitude is much larger than the energy spacing between the adiabatic curves in Figure 8a. But these two numbers cannot be directly compared, as the transformation between the adiabatic and the diabatic basis also involves the strong overlap within the non-orthogonal diabatic basis functions. The orthogonal projection coefficients of the $(6)^1\Sigma_g^+$ and $(5)^1\Sigma_g^+$ adiabatic states on the covalent and ionic channels are reproduced in Figures 8c and 8d, which illustrate how the adiabatic states exchange their ionic or covalent character at the avoided crossing. Beyond the crossing at large R, these coefficients reach values close to 0 or 1, while this trend is not so well visible before the crossing at small R. However, Figures 8c and 8d still suggest that the system can be conveniently described through a model involving only the two effective channels named by the limiting potentials $V_{\rm cov}$ and $V_{\rm ion}$, and interacting through a coupling term which can be taken roughly constant or slowly varying around their crossing.

The remaining part of this section is devoted to the definition of such a two-channel model.

5.2 The MFGH+OP method

In our two-channel problem, the system is described by two Schrödinger equations, coupled either by a radial interaction in an adiabatic picture, or by an electronic operator in a diabatic picture, and is solved using the MGFH method, described in detail in the references quoted above. We recall here only its basic features:

- the total Hamiltonian $\mathbf{H} = \mathbf{T} + \mathbf{V}$ for $p = 2$ coupled channels, where $\mathbf{T}$ and $\mathbf{V}$ are respectively the kinetic energy and potential energy operators, is represented by its matrix elements in a basis of N plane waves: $\exp(\mathrm{i}2\pi kR/L)$, $k = -((N/2)-1), ..., 0, ..., N/2$, where L is the length of a N point grid in the position coordinate R;
- the resulting $Np \times Np$ matrix is diagonalized, yielding all the eigenvalues and eigenvectors of the system;
- the grid step is adapted to the local de Broglie wavelength of the problem, which is equivalent to a change

of variable and to a transformation of wave functions, according to equations (2.9–2.11) of reference [23]. This procedure called mapping reduces substantially the number of required grid points, and enables the calculation of vibrational levels arbitrarily close to the dissociation limit and thus large R [30].

Calculations using the Fourier grid Hamiltonian representation without mapping have already been performed using the adiabatic representation of potential curves [22]. In contrast, the mapping procedure cannot be applied in the adiabatic picture, as the radial derivative operators are represented by a non-symmetric matrix [31]. This difficulty can be overcome in the diabatic representation. In the present work, all calculations are performed in the diabatic picture, which allows an easy implementation of the MFGH method.

The widths of the predissociated levels are calculated with the optical potential (OP) method [25–27], implemented into the MFGH method [28]. An optical potential $V_{\rm opt}$ is a pure imaginary potential placed at the outer border of the grid in the coordinate space, in order to ensure pure outgoing wave boundary conditions for the calculated wave functions. The Hamiltonian is now complex, and its diagonalization yields complex eigenvalues, whose real part corresponds to the position of the resonance, whereas the imaginary part provides half of the predissociation width. Following reference [32], we use for $V_{\rm opt}$ an exponential form:

$$V_{\rm opt} = A_{\rm opt} N_{\rm opt} \exp\left(\frac{-2L_{\rm opt}}{R - R_{\rm opt}}\right), \tag{3}$$

where $N_{\rm opt}$ is a normalization factor, $R_{\rm opt}$, $L_{\rm opt}$ and $A_{\rm opt}$ are respectively the position, the range, and the amplitude of the optical potential. We choose the parameter values recommended in reference [32]: $A_{\rm opt} = 0.002$ a.u. (1 a.u. = 219474.63137 cm^{-1}), $L_{\rm opt} = 12a_0$, $R_{\rm opt} = L - L_{\rm opt}$, $N_{\rm opt} = 13.22$. The convergence of the calculated widths is checked as described in reference [28].

5.3 The diabatization procedure for the two-channel problem

According to the arguments developed in paragraph 5.1, we set up a diabatization procedure restricted to our two-channel problem, which is different from the one including many channels developed in reference [29]. In the adiabatic basis, the radial Schrödinger equation is (in atomic units):

$$\left(-\frac{1}{2\mu}\frac{{\rm d}^2}{{\rm d}R^2} + V_{ii}^a\right)\psi_i - \frac{1}{2\mu}\sum_{j=1}^{2}\left(2\tau_{ij}^{(1)}\frac{\rm d}{{\rm d}R} + \tau_{ij}^{(2)}\right)\psi_j = E_i\psi_i. \tag{4}$$

We note hereafter V_{ii}^a and ψ_i the adiabatic potential and the radial wave function corresponding to channel i, E_i its energy, and μ the reduced mass of the molecule. The rotational term $l(l+1)/2\mu R^2$ is included in V_{ii}^a. The radial interactions $\tau_{ij}^{(1)}$ and $\tau_{ij}^{(2)}$ in the adiabatic picture are given by:

$$\tau_{ij}^{(1)}(R) = \left\langle \varphi_i^a(R,r) \left| \frac{\partial}{\partial R} \right| \varphi_j^a(R,r) \right\rangle \tag{5}$$

$$\tau_{ij}^{(2)}(R) = \left\langle \varphi_i^a(R,r) \left| \frac{\partial^2}{\partial R^2} \right| \varphi_j^a(R,r) \right\rangle, \tag{6}$$

where $\varphi_i^a(R,r)$ is the adiabatic electronic wave function associated to the channel i, depending on both R and on the electronic coordinates r. The brackets represent the integration over electronic coordinates. As a consequence of a two state model, in which $\tau^{(1)}$ is real, we have:

$$\tau_{ij}^{(1)}(R) = -\tau_{j,i}^{(1)}(R) = \tau^{(1)}(R) \tag{7}$$

$$\tau_{ii}^{(1)}(R) = 0. \tag{8}$$

The diabatic radial Schrödinger equation used in the MFGH method is:

$$\left(-\frac{1}{2\mu}\frac{{\rm d}^2}{{\rm d}R^2} + V_{ii}^d\right)\phi_i + \sum_j V_{ij}^d\phi_j = E_i\phi_i, \tag{9}$$

where ϕ_i is the diabatic wavefunction corresponding to channel i, V_{ii}^d are the diabatic potentials, and V_{ij}^d the electronic couplings. As previously, the rotational contribution is included in V_{ii}^d.

The diabatization procedure consists simply in a change of basis, through the transformation matrix $\mathbf{U}$:

$$\mathbf{V}^d = \mathbf{U}^{-1}\mathbf{V}^a\mathbf{U}, \tag{10}$$

where $\mathbf{V}^a$ and $\mathbf{V}^d$ are the potential operator matrices in the adiabatic and diabatic picture, respectively. In a two state model, the matrices $\mathbf{V}^d$, $\mathbf{V}^a$ and $\mathbf{U}$ have the following block structure:

$$\mathbf{V}^d = \begin{pmatrix} V_{11}^d & V_{12}^d \\ V_{21}^d & V_{22}^d \end{pmatrix}, \quad \mathbf{V}^a = \begin{pmatrix} V_{11}^a & 0 \\ 0 & V_{22}^a \end{pmatrix}, \quad \mathbf{U} = \begin{pmatrix} U_{11} & U_{12} \\ U_{21} & U_{22} \end{pmatrix}. \tag{11}$$

The matrix $\mathbf{U}$ is the solution of the differential equation written in a matrix form (see Appendix A):

$$\frac{{\rm d}\mathbf{U}}{{\rm d}R} = -\tau^{(1)}\mathbf{U}, \tag{12}$$

where $\tau^{(1)}$ is the matrix corresponding to the radial interactions $\tau_{i,j}^{(1)}(R)$. Equation (12) is equivalent to:

$$\begin{aligned} \frac{\partial}{\partial R}U_{11} &= -\tau^{(1)}(R)U_{21} \\ \frac{\partial}{\partial R}U_{21} &= \tau^{(1)}(R)U_{11} \\ \frac{\partial}{\partial R}U_{12} &= -\tau^{(1)}(R)U_{22} \\ \frac{\partial}{\partial R}U_{22} &= \tau^{(1)}(R)U_{12}. \end{aligned} \tag{13}$$

This 2×2 coupled equation system is solved using the Runge-Kutta algorithm [33]. Equation (10) provides then the diabatic potentials V_{ii}^d and the electronic interactions V_{ij}^d for all R. We performed inward integration over the length of the coordinate grid starting at the maximum value. The **U** matrix is initialized to the unity matrix for large internuclear distances. Other initial conditions lead to different diabatic representations. The advantage of the unity initialization is that it ensures that at large internuclear distances, interactions vanish and adiabatic and diabatic basis are equal, which is the best approach to the situation in Figures 8c and 8d.

We note that in the frame of a two-state model, the U matrix elements can also be found analytically provided the primitive of $\tau^{(1)}$ is known (see Appendix B).

5.4 Modeling of the adiabatic potentials and radial interactions

The analytic potential curve derived from the experiment, and the curve of reference [9] for the $(6)^1\Sigma_g^+$ outer well are close to each other, so we match the former curve to the adiabatic potential from reference [9] to ensure, that the calculated energy levels are close to the experimental ones. To deal with adiabatic potentials consistent with the definition of equation (4) we subtract the $\tau^{(2)}$ interaction from the experimental $(6)^1\Sigma_g^+$ potential, derived from the U matrix (see Appendix A). However, this term is found to be small and of no significant influence in our analysis. For the dissociation channel, we use the calculated adiabatic $(5)^1\Sigma_g^+$ potential of reference [9].

In our approach, the radial interaction $\tau^{(1)}$ between the adiabatic channels plays the role of an adjustable parameter. We tried two different shapes for its modeling:

– a Lorentzian function:

$$\tau_{LZ}^{(1)}(R) = \frac{A}{(R - R_c)^2 + \omega^2}, \qquad (14)$$

characterized by the position R_c and the width ω of the avoided crossing, and the interaction strength A. If $A = 4\omega^2$, this expression corresponds directly to a Landau-Zener model where the diabatic interaction is assumed constant and the difference between the two diabatic potentials is varying linearly. Taking A and ω^2 as independent parameters allows for a better flexibility of the model, to account for the slow asymmetric variation of the ionic-covalent coupling around the crossing suggested by Figure 8b, and for the possible inaccuracy of the $(5)^1\Sigma_g^+$ potential, which is kept fixed. In the following, we will refer to this case as the modified Landau-Zener model;

– an exponential function (in atomic units):

$$\tau_{\exp}^{(1)}(R) = \frac{-\alpha\dfrac{(R - Rc)}{RRc}\lambda\beta e^{(-\lambda R)} + \dfrac{\beta}{R^2}e^{(-\lambda R)}}{\left(\alpha\dfrac{(R - Rc)}{RRc}\right)^2 + 4(\beta e^{(-\lambda R)})^2}, \qquad (15)$$

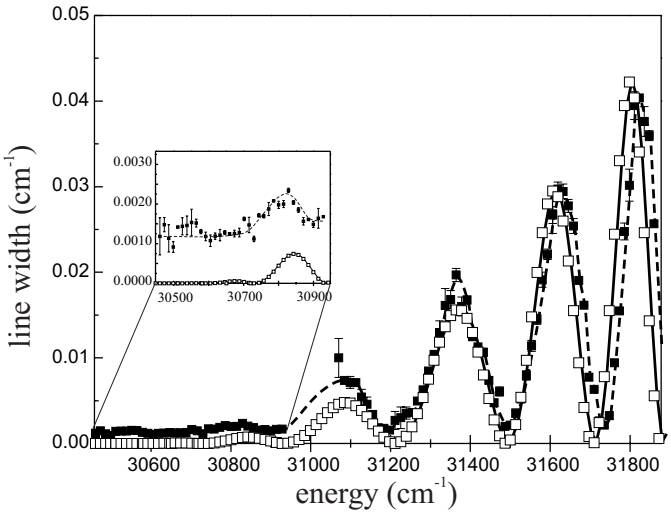

Fig. 9. Experimental (solid squares) and calculated (open squares) predissociation line widths of the vibrational levels (for $J_6 = 9$) lying in the $(6)^1\Sigma_g^+$ outer well, as a function of the energy. The parameters used are $R_c = 33.4a_0$, $\omega = 1.25a_0$, and $A = 0.55a_0$.

where β and λ characterize the strength of the exponential diabatic interaction, R_c is the position of the avoided crossing and α is the slope of the variation of the difference between the two diabatic potentials. Such an expression actually reflects the asymmetric behaviour of the ionic-covalent interaction over the range of distance shown in Figure 8b.

For each model, the parameters are adjusted in order to reproduce the experimental results.

5.5 Comparison between experiment and theory

We solved numerically the diabatic Schrödinger equation (9) with the MFGH+OP method, choosing the radial interaction represented in Figure 10a, with parameter values: $R_c = 33.4a_0$, $\omega = 1.25a_0$, $A = 0.55a_0$. The computed predissociation widths are displayed in Figure 9 for the modified Landau-Zener model, together with the experimental values. The oscillations of the widths with respect to the energy is a consequence of an interference effect between bound and continuum states. It can be understood as the variation of the relative phase of the two wave functions associated to each channel, in a Franck-Condon type formula [34]. Similar oscillations have recently been predicted in Cs_2 predissociation [28].

The diabatic curves deduced from our two-channel diabatization associated to the corresponding electronic interaction of Figure 10b are shown around the crossing region in Figure 11. The slight wiggles of the diabatic curves at the crossing point are not physical, and are not present in the curves of reference [29]. They reveal the limit of the present two-state model. Note also that the electronic interaction yielded by the modified Landau-Zener model, and the one from reference [29] have a similar variation,

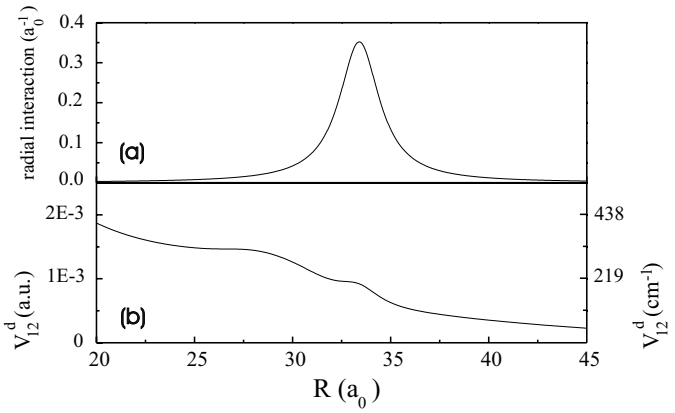

Fig. 10. (a) Radial interaction $\tau^{(1)}$ used for the modified Landau-Zener model. (b) Electronic interaction deduced from the two-channel diabatization procedure. Note that the symmetric radial interaction yields an asymmetric electronic interaction. The parameter values are the same as for Figure 9.

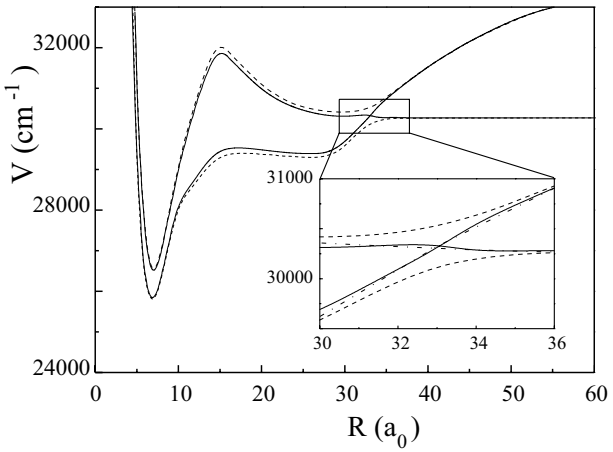

Fig. 11. Solid lines: calculated diabatic potentials V_{11}^d (or $V_{\rm cov}$) and V_{22}^d (or $V_{\rm ion}$), corresponding to the electronic interaction of Figure 10b. Dashed lines: adiabatic $(5)^1\Sigma_g^+$ and $(6)^1\Sigma_g^+$ potential curves. The inset shows also the diabatic curves of reference [29], as dot-dashed lines.

but the magnitude is roughly a factor 20 different, which is related to the definition of the electronic wave functions in reference [29], which are non-orthogonal.

Up to now the comparison between experiment and calculation was restricted to the linewidth oscillation. To improve the model description we will use a step by step iterative procedure for adjusting the shape of the outer well of the $(6)^1\Sigma_g^+$ state by alternating the comparison between level positions and widths.

A direct automatic fit using as intermediate step the MFGH+OP calculations and adjusting the potential and the coupling is feasible, but would require longer numerical calculations which are not necessary for the present discussion.

The coupling between the $(5)^1\Sigma_g^+$ and $(6)^1\Sigma_g^+$ states leads to the observed line widths due to predissociation, but also to a shift in the energetic positions of the levels. The determination of a potential for the external well of the $(6)^1\Sigma_g^+$ state directly from the measured energy level positions as described in Section 4 does not include the coupling. Therefore, using such a potential for the coupled channel calculation leads to calculated energies which deviate from the observed ones. In the case of the Lorentzian shaped coupling discussed above the deviations increase with increasing vibrational quantum number and reach values up to 0.4 cm^{-1} for $v_6 \approx 100$ values, *i.e.* 80 times the experimental uncertainty. The corresponding residuals are shown in Figure 5 as open circles.

In order to include the coupling in the potential determination we used the following strategy. For a set of coupling parameters which describes the observed line widths oscillation satisfactorily, we determined the energy shift introduced by this coupling in the coupled channel calculation. Then again a single-channel potential fit for the outer well was done, but using now energy positions which are shifted compared to the measured ones by just the amount the coupling introduces. The quality of this potential fit is not changed compared to the final result obtained in Section 4, *i.e.* $\sigma = 2.1$.

Starting with this new potential, we performed again a coupled channel calculation using the same coupling as before. We found that only a slight adjustment of the coupling parameters is necessary to obtain agreement between observation and simulation which is as good for the widths as the earlier one or better for low lying vibrational levels up to $v_6 \approx 65$. The variation of (obs-cal) was now similar to the one obtained with the single potential fit. For vibrational levels higher than $v_6 \approx 80$ the values for (obs-cal) increased again up to -0.2 cm^{-1} for $v_6 \approx 100$. The truncated power expansion in its present form is probably not flexible enough to account for the potential turnover to form the potential barrier. This systematic deviation could be removed by adjusting the change from analytic to the *ab initio* potential in this region more carefully with respect to the eigenenergies. The best obtained result is shown in Figure 5.

To set up a fitting procedure for a double well potential would not solve the problem because there are no experimental data available for levels of the inner well which are located close to the barrier. The coefficients of the obtained potential are listed in Table 1. Oscillations of (obs-cal) similar to the line widths, as observed for the single channel case (black squares in Fig. 5) are still visible in the coupled channel result (open squares).

We performed a further check of our two channel model according to the following lines: we verified that the electronic interaction in Figure 8b is well represented by the exponential form $\beta \exp(-\lambda R)$ with the following parameters: $\beta = 0.725 a_0^{-1}$, $\lambda = 0.102 a_0^{-1}$. Using then the exponential model of equation (15), we obtained results for the widths and for the potential, which were indistinguishable from the modified Landau-Zener results at the scale of Figures 9 and 11. The parameter values are $\alpha = 1$, $\beta = 0.014 a_0^{-1}$, $R_c = 32 a_0$, $\lambda = 0.1 a_0^{-1}$. The corresponding diabatic potentials are also very close to this previous model. This is consistent with the slow variation of the diabatic electronic interaction over the crossing point

Table 1. Parameters used for the outer well of the $(6)^1\Sigma_g^+$ potential. The range of validity is $17.2a_0$ to $40.1a_0$. The a_i parameters are in cm^{-1}, R_m in a_0 units, and b is dimensionless. In order to faithfully represent the potentials, coefficients are given to eighteen significant digits. It does not reflect the accuracy of the potentials in reproducing experimental energies.

R_m	$29.69872143a_0$
b	0.28
T_m	30417.04650532
a_1	$0.147225873174429509 \times 10^2$
a_2	$0.101443258703711126 \times 10^5$
a_3	$0.427251930141305493 \times 10^5$
a_4	$0.213878195489583799 \times 10^6$
a_5	$0.310481409886057163 \times 10^7$
a_6	$0.514625912878118157 \times 10^8$
a_7	$0.109287568874845281 \times 10^9$
a_8	$-0.452319092394113731 \times 10^{10}$
a_9	$-0.316148446444594040 \times 10^{11}$
a_{10}	$0.116099607761238815 \times 10^{12}$
a_{11}	$0.177795748946080981 \times 10^{13}$
a_{12}	$0.154533352265548633 \times 10^{13}$
a_{13}	$-0.464244470443060859 \times 10^{14}$
a_{14}	$-0.161574306316988438 \times 10^{15}$
a_{15}	$0.507427546857114000 \times 10^{15}$
a_{16}	$0.393752682633147900 \times 10^{16}$
a_{17}	$0.228002714748274850 \times 10^{16}$
a_{18}	$-0.411969000045946720 \times 10^{17}$
a_{19}	$-0.116942344234640384 \times 10^{18}$
a_{20}	$0.798368231578501760 \times 10^{17}$
a_{21}	$0.992010575143279616 \times 10^{18}$
a_{22}	$0.173307403192511334 \times 10^{19}$
a_{23}	$-0.867084271692733312 \times 10^{18}$
a_{24}	$-0.844881449493068083 \times 10^{19}$
a_{25}	$-0.157821110721069363 \times 10^{20}$
a_{26}	$-0.152630398106187428 \times 10^{20}$
a_{27}	$-0.791415921838104678 \times 10^{19}$
a_{28}	$-0.175141383886510976 \times 10^{19}$

region ($\approx 2a_0$ wide), which is similar in both determinations. The value used for β is 50 times smaller than the value deduced from Figure 8. This difference is comparable to the difference between the splitting of the two adiabatic curves and the electronic interaction both given in Figure 8. Allowing an adjustable value of β is equivalent to taking into account the strong overlap integrals involved in the electronic interaction of the extended diabatization procedure from reference [29].

6 Conclusion

We have investigated experimentally and theoretically the outer well of the $(6)^1\Sigma_g^+$ state of Na_2 dimer. The observed oscillating behavior with respect to the widths of the predissociated levels is well described in the frame of a two state model in which the $(6)^1\Sigma_g^+$ is perturbed by the lower $(5)^1\Sigma_g^+$ *via* a non Born-Oppenheimer interaction. The MFGH+OP method was used and appears to be very powerful for the study of such molecular dynamics. A fit of an analytic potential of the outer well has been done providing a potential which reproduces experimental values with a standard deviation of $\sigma = 2.1$ for the energy positions and qualitatively good agreement for the widths of the predissociated levels. But residual oscillations of the energetic positons which follow synchronously the oscillations of the widths still remain. This probably indicates that the coupling and/or the potential forms with respect to the internuclear separations are not sufficiently flexible for the present case.

In total, this opens the way for a promising spectroscopic molecular potential determination which takes into account not only the energy shift due to the perturbation but also the predissociation widths of the perturbed levels. Beyond spectroscopic interest, the study of the external wells of dimer potentials is of particular interest in the search of efficient cold molecule formation scheme, although predissociation effects may substantially reduce the efficiency of the cold molecule formation process.

This work was supported by the Deutsche Forschungsgemeinschaft within the SFB 407 and by the PROCOPE program between Germany and France. P.P., O.D., and F.M. thank the team of Prof. Tiemann for friendly hospitality in Hannover. Computation time from the Institut du Développement et des Ressources en Informatique Scientifique (IDRIS, France) is gratefully acknowledged.

Appendix A: derivation of the differential equation (12)

We start with the adiabatic Schrödinger equation (Eq. (4)) that we rewrite in the compact form as:

$$\mathbf{H}^a\psi = E\psi \tag{16}$$

with $\mathbf{H}^a$ the Hamiltonian operator given in equation (4).

If we apply to this equation the transformation $\mathbf{U}$ so that $\psi = \mathbf{U}\phi$ then we have:

$$\mathbf{U}^{-1}\mathbf{H}^a\mathbf{U}\phi = E\phi \tag{17}$$

where the new operator $\mathbf{U}^{-1}\mathbf{H}^a\mathbf{U} = \mathbf{H}^d$ is the Hamiltonian operator expressed in the diabatic representation.

Starting with equation (4) in a two state approximation ($\tau_{ij} \to \tau$), we have for $\mathbf{H}^d$:

$$\begin{aligned}\mathbf{H}^d = -\frac{1}{2\mu}\Bigg(&\frac{\partial^2}{\partial R^2} + 2\left(\mathbf{U}^{-1}\mathbf{U}' + \mathbf{U}^{-1}\tau^{(1)}\mathbf{U}\right)\frac{\partial}{\partial R} \\ &+ \mathbf{U}^{-1}\mathbf{U}'' + 2\mathbf{U}^{-1}\tau^{(1)}\mathbf{U}' \\ &+ \mathbf{U}^{-1}\tau^{(2)}\mathbf{U} - 2\mu\mathbf{U}^{-1}\mathbf{V}^a\mathbf{U}\Bigg)\end{aligned} \tag{18}$$

with $\mathbf{U}'$ and $\mathbf{U}''$ respectively the first and second derivative of $\mathbf{U}$ with respect to R.

If we compare this last expression to the equation (9) we must have:

$$\mathbf{U}^{-1}\mathbf{U}' + \mathbf{U}^{-1}\tau^{(1)}\mathbf{U} = 0 \tag{19}$$

and

$$\mathbf{U}^{-1}\mathbf{U}'' + 2\mathbf{U}^{-1}\tau^{(1)}\mathbf{U}' + \mathbf{U}^{-1}\tau^{(2)}\mathbf{U} = 0 \tag{20}$$

which leads to the desired equations for $\tau^{(1)}$ and $\tau^{(2)}$, which should be fulfilled simultaneously:

$$\tau^{(1)} = -\mathbf{U}'\mathbf{U}^{-1} \tag{21}$$

$$\tau^{(2)} = -\mathbf{U}(\mathbf{U}'')^{-1}. \tag{22}$$

From equation (21) $\mathbf{U}$ can be determined. Finally we have:

$$\mathbf{H}^d = -\frac{1}{2\mu}\left[\frac{\partial^2}{\partial R^2} - \mathbf{U}^{-1}\left(2\mu\mathbf{V}^a + \bar{\tau}^{(2)}\right)\mathbf{U}\right] \tag{23}$$

where $\bar{\tau}^{(2)}$ is constructed to fulfill equation (20).

Appendix B: derivation of the analytic formula for the matrix element of U

We recall here the general formulation of a transformation between a diabatic and an adiabatic representation of molecular states, expressed as a rotation with an angle $\theta(R)$ in a two-state configuration space. The rotation matrix is expressed as:

$$U(R) = \begin{pmatrix} \cos\theta(R) & -\sin\theta(R) \\ \sin\theta(R) & \cos\theta(R) \end{pmatrix}. \tag{24}$$

We note $\varphi_I^a(R)$ and $\varphi_{II}^a(R)$ the adiabatic electronic states and φ_I^d and φ_{II}^d the diabatic states. The adiabatic basis depend on the internuclear distances R whereas the diabatic basis is R independent.

We pass from one basis to another with the $\mathbf{U}$ matrix so that:

$$\varphi_I^d = \cos\theta\varphi_I^a(R) - \sin\theta\varphi_{II}^a(R) \tag{25}$$

$$\varphi_{II}^d = \sin\theta\varphi_I^a(R) + \cos\theta\varphi_{II}^a(R). \tag{26}$$

After derivation of the first equation with respect to R and after projection over $\langle\varphi_{II}^a(R)|$, we obtain if we assume that the adiabatic basis is orthonormal:

$$\frac{\partial\theta}{\partial R} = \left\langle \varphi_{II}^a(R)\left|\frac{\partial}{\partial R}\right|\varphi_I^a(R)\right\rangle = \tau^{(1)} \tag{27}$$

so that

$$\theta = \int \tau^{(1)}(R)\mathrm{d}R. \tag{28}$$

If

$$\tau^{(1)}(R) = \tau_{LZ}^{(1)}(R) = \frac{A}{(R-R_c)^2 + \omega^2} \tag{29}$$

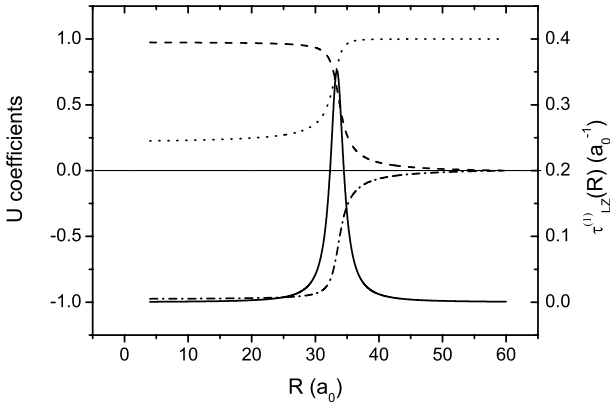

Fig. 12. U_{11} (dotted line), U_{21} (dashed line) and U_{12} (dot-dashed line) matrix elements of $\mathbf{U}$ in the case of a Lorentzian radial (solid line) interaction with the same parameters as in Figure 9.

the former equation can be integrated analytically, we obtain:

$$\int \tau^{(1)}(R)\mathrm{d}R = \frac{A}{\omega}\left(\mathrm{arctg}\left(\frac{R-R_c}{\omega}\right) - \mathrm{arctg}\left(\frac{-R_c}{\omega}\right)\right) \tag{30}$$

and for the matrix coefficients we have:

$$U_{11} = U_{22} = \cos\left[\frac{A}{\omega}\left(\mathrm{arctg}\left(\frac{R-R_c}{\omega}\right) - \mathrm{arctg}\left(\frac{-R_c}{\omega}\right)\right)\right] \tag{31}$$

$$U_{21} = -U_{12} = \sin\left[\frac{A}{\omega}\left(\mathrm{arctg}\left(\frac{R-R_c}{\omega}\right) - \mathrm{arctg}\left(\frac{-R_c}{\omega}\right)\right)\right]. \tag{32}$$

Figure 12 shows the numerical solution of equation (12) for the same parameters as in Figure 9, it is identical to the analytical formulas developed in the present appendix.

References

1. J. Vergès, C. Effantin, J. d'Incan, D.L. Cooper, R.F. Barrow, Phys. Rev. Lett. **53**, 46 (1984)
2. A. Pashov, W. Jastrzebski, W. Jaśniecki, V. Bednarka, P. Kowalczyk, J. Mol. Spectrosc. **203**, 264 (2000)
3. W. Jastrzebski, W. Jaśniecki, P. Kowalczyk, R. Nadyak, A. Pashov, Phys. Rev. A **62**, 042509 (2000)
4. W. Jastrzebski, A. Pashov, P. Kowalczyk, J. Chem. Phys. **114**, 10725 (2001)
5. A. Fioretti, D. Comparat, A. Crubellier, O. Dulieu, F. Masnou-Seeuws, P. Pillet, Phys. Rev. Lett. **80**, 4402 (1998)
6. P.D. Lett, K. Helmerson, W.D. Philips, L.P. Ratliff, S.L. Rolston, M.E. Wagshul, Phys. Rev. Lett. **71**, 2200 (1993)

7. F.K. Fatemi, K.M. Jones, P.D. Lett, E. Tiesinga, Phys. Rev. A **66**, 053401 (2002)
8. C. Gabbanini, A. Fioretti, A. Lucchesini, S. Gozzini, M. Mazzoni, Phys. Rev. Lett. **84**, 2814 (2000)
9. S. Magnier, Ph. Millié, O. Dulieu, F. Masnou-Seeuws, J. Chem. Phys. **98**, 7113 (1993)
10. C.-C. Tsai, J.T. Bahns, W.C. Stwalley, J. Mol. Spectrosc. **167**, 429 (1994)
11. M.-L. Almazor, O. Dulieu, M. Elbs, E. Tiemann, F. Masnou-Seeuws, Eur. Phys. J. D **5**, 237 (1999)
12. E. Tiemann, H. Knöckel, H. Richling, Z. Phys. D **37**, 323 (1996)
13. M. Elbs, T. Laue, H. Knöckel, E. Tiemann, Phys. Rev. A **59**, 3665 (1999)
14. H. Wang, private communication, 1998
15. `http://www.toptica.com/products/iodinespec/`, Program *IodineSpec* (2001)
16. M. Vatasecu, O. Dulieu, C. Amiot, D. Comparat, C. Drag, V. Kokoouline, F. Masnou-Seeuws, P. Pillet, Phys. Rev. A **61**, 044701 (2000)
17. C. Samuelis, E. Tiesinga, T. Laue, M. Elbs, H. Knöckel, E. Tiemann, Phys. Rev. A **63**, 012710 (2000)
18. C.C. Martson, G.G. Balint-Kurti, J. Chem. Phys. **91**, 3571 (1989)
19. D.T. Colbert, W.H. Miller, J. Chem. Phys. **96**, 1892 (1992)
20. M. Monnerville, J.M. Robbe, J. Chem. Phys. **101**, 7580 (1994)
21. O. Dulieu, P.S. Julienne, J. Chem. Phys. **103**, 60 (1995)
22. M. Monnerville, J.M. Robbe, Eur. Phys. J. D **5**, 381 (1999)
23. V. Kokoouline, O. Dulieu, R. Kosloff, F. Masnou-Seeuws, J. Chem. Phys. **110**, 9865 (1999)
24. V. Kokoouline, O. Dulieu, R. Kosloff, F. Masnou-Seeuws, Phys. Rev. A **62**, 032716 (2000)
25. G. Jolicard, E.J. Austin, Chem. Phys. Lett. **121**, 106 (1985)
26. E.J. Austin, G. Jolicard, Chem. Phys. **103**, 295 (1986)
27. C. Leforestier, E.J. Austin, G. Jolicard, J. Chem. Phys. **88**, 1026 (1988)
28. P. Pellegrini, O. Dulieu, F. Masnou-Seeuws, Eur. Phys. J. D **20**, 77 (2002)
29. S. Magnier, M. Aubert-Frécon, O. Bouty, F. Masnou-Seeuws, Ph. Millié, V.N. Ostrovskii, J. Phys. B **27**, 1723 (1994)
30. Kai Willner, O. Dulieu, F. Masnou-Seeuws, J. Chem. Phys. (in press)
31. M. Vatasescu, Ph.D. thesis, Université Paris-Sud, 1999
32. Á. Vibók, G.G. Balint-Kurti, J. Phys. Chem. **96**, 8712 (1992)
33. W.H. Press, S.A. Teukolsky, W.T. Vetterling, B.P. Flannery, *Numerical recipes* (Cambridge University Press, 1992)
34. G. Herzberg, *Molecular Spectra and Molecular Structure: Spectra of Diatomic Molecules* (Van Nostrand Reinhold, 1950)